CIVIL ENGINEERING JOURNAL

Article no. 31

THE CIVIL ENGINEERING JOURNAL 4-2025

THE INFLUENCE OF END EFFECTS ON THE FLOW RESISTANCE CHARACTERISTICS OF VARIABLE DIAMETER CYLINDERS

Meng Zhao[1], Yaning Duan[1], Xingbo Lan[1] and Zile Jia[2]

1. *College of Energy and Power Engineering, Inner Mongolia University of Technology, Hohhot 010080, China, email: 1530991045@qq.com*
2. *College of Civil Engineering, Inner Mongolia University of Technology, Hohhot 010051 China*

Received: 29.05.2024
Received in revised form: 16.07.2025
Accepted: 06.11.2025

ABSTRACT

Based on the study of the flow around finite-length cylinders, an analysis of the flow resistance characteristics of commonly encountered variable diameter cylinders at high Reynolds numbers was conducted. A comprehensive relationship equation for the flow resistance within the subcritical region, the drag crisis region, and the drag recovery region was obtained. Additionally, the influence of end effects on the flow resistance characteristics of finite-length cylinders and variable diameter cylinders was analyzed using large eddy simulation (LES), and a comprehensive formula describing the range of end effect influence was obtained. The results indicate that the flow resistance coefficients at both ends of the variable diameter cylinder are influenced by the aspect ratio λ, Reynolds number (Re), and included angle θ. As θ and λ increase, the distance affected at the top of the cylinder increases. As Re decreases, the affected distances at the top and bottom increase. The comprehensive formula for the influence range can be used to modify the relationship equation for the drag coefficient. These findings have important implications for the study and application of the flow characteristics of finite-length variable diameter cylinders.

KEYWORDS

Variable-diameter Cylinders, Aspect Ratio, Flow Field, High Reynolds Number, End-Face Effect

INTRODUCTION

The flow dynamics around cylindrical bodies have long been a subject of intensive research due to their relevance in engineering applications, including offshore structures, heat exchangers, and fluid transport systems. While traditional studies often focused on uniform-diameter, infinitely long cylinders, real-world applications frequently involve finite-length, variable-diameter geometries, such as tapered

columns and truncated cones. These configurations introduce additional complexities, particularly related to end effects and axial geometry variation. Recent studies have highlighted how structural modifications—such as end shaping [1] or proximity to walls [2] —can drastically alter flow resistance and vortex shedding characteristics. The influence of geometry is further evident in the behavior of dual-step and tandem cylinders. For example, Morton and Yarusevyc [3] revealed distinct wake modes due to diameter discontinuities, while Wang et al. [4] and Gu et al. [5] showed how diameter ratio and spacing affect flow-induced vibrations and shielding effects. Multiphase flows, as investigated by Khan et al [6], also demonstrate that diameter variation leads to asymmetric hydrodynamic loads due to buoyancy and wake interactions. Despite these insights, the combined effects of variable diameter, finite length, and axial tapering have received comparatively little attention. In particular, the quantification of end-face effects on drag coefficient distribution and their integration into predictive models remains limited. This study aims to bridge this gap by employing high-fidelity Large Eddy Simulation (LES) to analyze the flow resistance of finite-length variable diameter cylinders across various Reynolds number regimes. We propose a segmented drag coefficient model and a correction formula to account for end effects, offering enhanced predictive capabilities for practical engineering applications.

The flow around cylinders and variable-diameter cylinders is a prevalent phenomenon in engineering, characterized by fluctuating separation points and the formation of trailing and shedding vortices, especially under high Reynolds number conditions, resulting in highly complex flow characteristics [7]-[13].While there are certain similarities between the flow around cylinders and variable-diameter cylinders, significant differences also exist. Scholars both domestically and internationally have conducted numerous experiments and numerical simulations to study the distribution of flow resistance for finite-length cylinders with various aspect ratios. For instance, reference [14] , through model experiments and comparative analyses with references [14] ($5.2\times10^4 \le Re \le 9.4\times10^4$),references [15] ($1.25\times10^5 \le Re \le 2.09\times10^5$),and reference [16]-[18] ($Re \ge 1.2\times10^5$), provided the variation patterns of the flow resistance coefficients of cylinders with different aspect ratios as a function of Reynolds number. Kravchenko and Moin employed large eddy simulation methods to analyze key issues in flow dynamics [19] . However, research on the flow characteristics of finite-length variable-diameter cylinders (such as truncated cones and frustums) is limited, lacking analysis of resistance fluctuation characteristics, key influencing factors of flow characteristics, and comprehensive relationship equations. Particularly, there is a lack of analysis regarding end-face effects, with insufficient exploration of the various influencing factors of end effects. Therefore, it is necessary to conduct relevant studies to establish a foundation for engineering applications. If the angle between the side characteristic line and the axis of the variable-diameter cylinder (θ) is small or the height of the cylinder is large, relevant theories and research findings on cylindrical flow can be utilized. Through appropriate methods to analyze and correct errors caused by end-face effects, the resistance characteristics of variable-diameter cylinder flow can be obtained.

Variable-diameter cylindrical structures are commonly found in practical engineering scenarios, including the arms of high-speed train pantographs and utility poles. These components experience cross-flow wind loading under operating

conditions and exhibit significant end-face effects due to their finite length and geometry. Figure 1 presents two real-world examples of such structures, further motivating the need to understand their drag characteristics in varying Reynolds regimes.

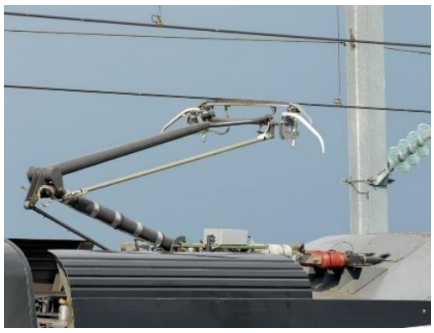

(a) overhead railway pantograph arm with tapered geometry

(b) tapered utility pole subjected to cross-flow wind

Fig. 1 - Examples of variable-diameter cylindrical structures in engineering application

THE DRAG COEFFICIENT OF FINITE-LENGTH CYLINDERS IN FLOW

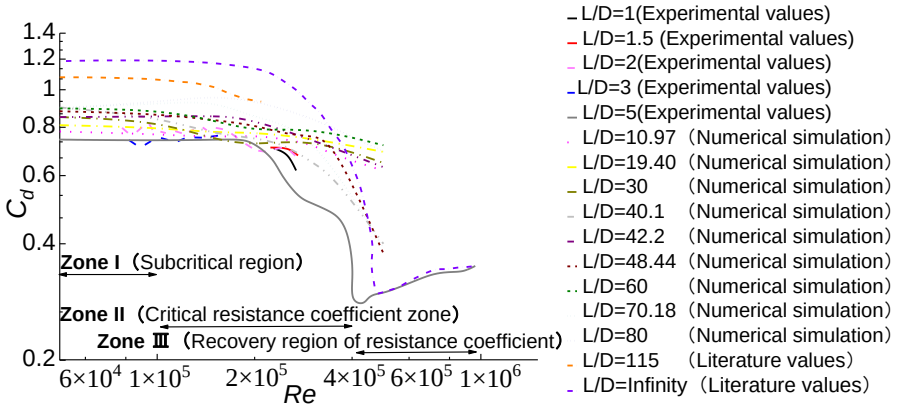

Fig. 2 - Variation of the drag coefficient of cylindrical flow with aspect ratio and Reynolds number. (Data partially compiled from references [19] and [20], combined with the authors' numerical simulations and fitted into three distinct flow regimes.)

To derive the resistance calculation formula for variable-diameter cylinders, it is necessary to first use numerical simulation methods to calculate the variation of the drag coefficient of cylinders with Reynolds number and aspect ratio. Therefore, corresponding cylinder models are established to calculate the average drag coefficient C_d, with aspect ratios λ ($\lambda = H/D$) ranging from 10 to 80. To cover both large and small aspect ratios, references [19] for infinite-length cylinders and finite-length cylinders with λ = 5,115, and references [20] for finite-length cylinders with λ =1,1.5,2,3 are cited. Through numerical calculations, the variation of the drag coefficient of cylinders with aspect ratio λ and Reynolds number Re is obtained, as shown in Figure 2.

The results of numerical simulations define three zones for the drag coefficient: within the subcritical region ($10^4 \le Re < 10^5$), within the drag crisis region ($10^5 \le Re < 4\times10^5$), and within the drag recovery region ($Re \ge 4\times10^5$). The comprehensive relationship equation for the drag coefficient of finite-length cylinders is fitted within these zones, represented in segments as follows [21] :

(1) When $10^4 \le Re < 10^5$, the subcritical region

$$C_d = 0.855 + 0.683\ln(Re) - 0.588\ln^2(Re) - 1.730\lambda + 2.629\lambda^2 \quad (1)$$

(2) When $10^5 \le Re < 4\times10^5$, the drag crisis region

$$C_d = 1.111 - 0.081\ln(Re) - 0.019\ln^2(Re) + 0.002\ln^3(Re) - 1.762\lambda + 3.987\lambda^2 - 2.381\lambda^3 \quad (2)$$

(3) When $Re \ge 4\times10^5$,the drag recovery region.

$$C_d = 0.739 - 0.124\ln(Re) + 0.009\ln^2(Re) + 7.510\lambda - 3.806\lambda^2 \quad (3)$$

DERIVATION OF THE DRAG COEFFICIENT FOR FINITE-LENGTH VARIABLE DIAMETER CYLINDER

The height of the variable diameter cylinder is denoted by H, with the top referred to as the upper base and the bottom referred to as the lower base. The diameters are represented by d_1 and d_2, and the radius are denoted by r_1 and r_2. In calculations, the diameter at the axisymmetric plane, known as the mid-diameter, denoted by D, is commonly used. The angle between the side characteristic line and the central axis is represented by θ. It is worth noting that variable diameter cylinders differ from cones and frustums, typically referring to various structural members in engineering with relatively small diameters and large aspect ratios. θ varies within very small angles, as shown in Figure 3.

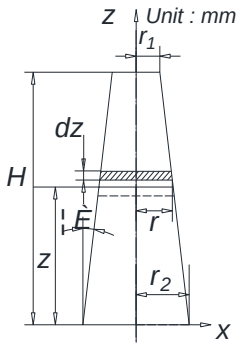

Fig. 3 - The drag coefficients for each section when Re=10^5.

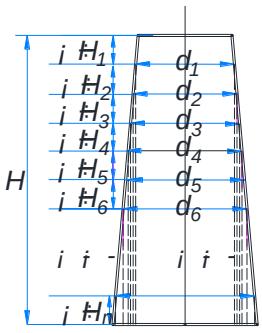

Fig. 4 - Definition of Variable Diameter Cylinder.

Suppose the variable diameter cylinder consists of n cylindrical sections, each with a height ΔH_1, diameter d_1, length ΔH_2 , diameter d_2, ... , height ΔH_n , diameter d_n. Let the aspect ratio be λ, $\lambda = H/D = H/(r_1 + r_2)$,and the mid-diameter of the variable diameter cylinder be D , $D = (d_1 + d_2)/2 = r_1 + r_2$, $\tan\theta = (r_2 - r_1)/H$ .Take a differential segment of length dz with a distance C_d from the bottom of the variable diameter cylinder, and a radius C_{pb} for the differential segment, as shown in Figure 4.

The resultant force acting on the cylinder is:

$$\sum F_{xi}=\frac{1}{2}\rho V^2\Delta H\left(C_{d1}d_1+C_{d2}d_2+...+C_{dn}d_n\right)=\frac{1}{2}\rho V^2\Delta H\sum C_{di}d_i \tag{4}$$

The drag force acting on this differential segment is:

$$\mathrm{d}F=C_d\frac{1}{2}\rho V^2\mathrm{d}A=C_d\rho V^2r\mathrm{d}z \tag{5}$$

$$F_x=\int_0^H C_d\rho V^2x\mathrm{d}z=\rho V^2\int_0^H C_dr\mathrm{d}z \tag{6}$$

Wherein:

$$C_d=f\left(\frac{H}{D},Re\right)=f\left(\lambda,Re\right)\ ,\ \ Re=\frac{VD}{\nu}$$

From $\tan\theta=\frac{r_2-r}{z}=\frac{r-r_1}{H-z}$, we obtain $r_2=\frac{(r-r_1)z}{H-z}+r$, hence:

$$r=\frac{D}{2}+\left(\frac{H}{2}-z\right)\tan\theta \tag{7}$$

Therefore, the expression for the drag force is:

$$F_x=\int_0^H C_d\rho V^2\left[\frac{D}{2}+\left(\frac{H}{2}-z\right)\tan\theta\right]dz \tag{8}$$

The expression for the drag coefficient is:

$$C_d=\frac{\int\frac{1}{2}\rho v^2\Sigma\left(C_{di}\Delta H_id_i\right)}{\frac{1}{2}\rho v^2HD}=\frac{\int\Sigma\left(C_{di}\Delta H_id_i\right)}{HD} \tag{9}$$

Integrating the segmented drag coefficients derived from Equations (1), (2), and (3) for flow around cylinders, we obtain the expressions for the drag of the variable diameter cylinder within different Reynolds number ranges, respectively:

(1) When $10^4\le Re<10^5$, the subcritical region

$$F_{x1}=\rho v^2\left\{\left[0.855+0.683\ln\left(Re\right)-0.588\ln^2\left(Re\right)-1.730\lambda+2.629\lambda^2\right]\left[\left(\frac{D}{2}+\frac{H}{2}\tan\theta\right)H-\tan\theta\frac{H^2}{2}\right]\right\} \tag{10}$$

(2) When $10^5\le Re<4\times10^5$, the drag crisis region

$$F_{x2}=\rho v^2\left\{\left[\begin{matrix}1.111-0.081\ln\left(Re\right)-0.019\ln^2\left(Re\right)+0.002\ln^3\left(Re\right)\\-1.762\lambda+3.987\lambda^2-2.381\lambda^3\end{matrix}\right]\left[\left(\frac{D}{2}+\frac{H}{2}\tan\theta\right)H-\tan\theta\frac{H^2}{2}\right]\right\} \tag{11}$$

(3) When $Re\ge4\times10^5$, the drag recovery region

$$F_{x3}=\rho v^2\left\{\left[0.739-0.124\ln\left(Re\right)+0.009\ln^2\left(Re\right)+7.510\lambda-3.806\lambda^2\right]\left[\left(\frac{D}{2}+\frac{H}{2}\tan\theta\right)H-\tan\theta\frac{H^2}{2}\right]\right\} \tag{12}$$

The expressions for the drag coefficient of the variable diameter cylinder within the three Reynolds number ranges are as follows:

(1) When $10^4\le Re<10^5$, the subcritical region

$$C_{d1}=\frac{2}{HD}\left\{\left[0.855+0.683\ln\left(Re\right)-0.588\ln^2\left(Re\right)-1.730\lambda+2.629\lambda^2\right]\left[\left(\frac{D}{2}+\frac{H}{2}\tan\theta\right)H-\tan\theta\frac{H^2}{2}\right]\right\} \tag{13}$$

(2) When $10^5\le Re<4\times10^5$, the drag crisis region

$$C_{d2}=\frac{2}{HD}\left\{\left[\begin{matrix}1.111-0.081\ln\left(Re\right)-0.019\ln^2\left(Re\right)+0.002\ln^3\left(Re\right)\\-1.762\lambda+3.987\lambda^2-2.381\lambda^3\end{matrix}\right]\left[\left(\frac{D}{2}+\frac{H}{2}\tan\theta\right)H-\tan\theta\frac{H^2}{2}\right]\right\} \tag{14}$$

(3) When $Re \geq 4\times10^5$, the drag recovery region

$$C_{d3}=\frac{2}{HD}\left\{\left[0.739-0.124\ln\left(Re\right)+0.009\ln^2\left(Re\right)+7.510\lambda-3.806\lambda^2\right]\left[\left(\frac{D}{2}+\frac{H}{2}\tan\theta\right)H-\tan\theta\frac{H^2}{2}\right]\right\} \quad (15)$$

THE INFLUENCE OF END-FACE EFFECTS ON THE CHARACTERISTICS OF DRAG FLUCTUATIONS

Large Eddy Simulation (LES) method

The Large Eddy Simulation (LES) method is highly accurate for solving flow around cylinders and similar bodies. Thus, LES is used to analyze the end-face effects of finite-length and variable diameter cylinders [22] .In LES, a box-filtering function filters the Navier-Stokes equations. The incompressible fluid Navier-Stokes equations are expressed as:

$$\frac{\partial\overline{\boldsymbol{u}}_{\boldsymbol{i}}}{\partial t}+\frac{\partial\left(\overline{\boldsymbol{u}}_{\boldsymbol{i}}\overline{\boldsymbol{u}}_{\boldsymbol{j}}\right)}{\partial x_j}=-\frac{1}{\rho}\frac{\partial\overline{p}}{\partial x}+\nu\frac{\partial^2\overline{\boldsymbol{u}}_{\boldsymbol{j}}}{\partial x_i\partial x_j}-\frac{\partial\overline{\tau}_{ij}}{\partial x_j} \quad (16)$$

$$\frac{\partial\overline{\boldsymbol{u}}_{\boldsymbol{i}}}{\partial x_i}=0,\mathrm{i}\in\left\{1,2,3\right\} \quad (17)$$

In the equation: x_i and x_j represent Cartesian coordinates, $\overline{\boldsymbol{u}}_{\boldsymbol{i}}$ and $\overline{\boldsymbol{u}}_{\boldsymbol{j}}$ represent filtered velocity vectors, where $i,j=x,y,z$ in three-dimensional problems; $\overline{p}$ denotes the pressure exerted on the fluid; ρ represents fluid density; ν denotes fluid viscosity. The right-hand side of the equation contains the unclosed term $\rho\overline{u_iu_j}-\rho\overline{u_i}\,\overline{u_j}$, referred to as the subgrid-scale stress τ_{ij} , where $t_{ij}=\rho\overline{u_iu_j}-\rho\overline{u_i}\,\overline{u_j}$.

Tab. 1 - The computational results of Large Eddy Simulation for flow around cylinders

	C_d	C_{pb}	St	θ_{sep}	L_{red}
Experiment	0.99±0.05	0.88±0.05	0.215±0.005	86.0º±2º	1.4D±0.01
High-order upwind	1.00	0.95	0.203	85.8	1.36D
Central conservation	1.00	0.93	0.207	86.9	1.40D
B-Spline	1.04	0.94	0.210	88.0	1.35D
This article	1.01	0.95	0.208	86.8	1.39D

Flow around a cylinder at a Reynolds number of 3900 is a typical subcritical flow. There are abundant experimental results available for this Reynolds number, which can be used for comparison to validate the accuracy of numerical simulation methods. When using high-precision schemes, the Stanford Turbulence Research Center experimented with high-precision upwind schemes, second-order conservative centered differencing schemes, and B-Spline Galerkin methods, all yielding satisfactory results. The length of the computational domain L is determined based on the streamwise wavelength of the near-wake flow structures from existing experimental results, where $L=\pi D$. The number of grids is 9.76 million. The numerical simulation results in Table 1 show good agreement with the experimental

results. In the table, C_d represents the drag coefficient, C_{pb} represents the pressure coefficient at the lee side point, St represents the Strouhal number, θ represents the separation angle, and L_{red} represents the length of the reattachment region.

To validate the reliability of the LES method used in this study, we replicated the well-documented flow condition at Reynolds number Re = 3900. This subcritical regime has been widely studied experimentally, and the simulation results from this work—such as drag coefficient (C_d), separation angle, and Strouhal number—showed good agreement with benchmark data. The comparison is detailed in Table 1, confirming that the simulation methodology accurately captures the critical flow features necessary for modeling more complex geometries.

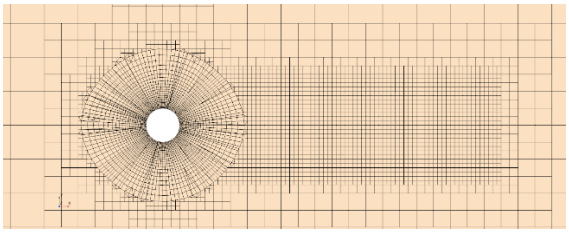

Fig. 5 - Computational grid for LES validation case at Re = 3900.

The computational domain was discretized using a structured mesh, structured mesh near the cylinder surface ensures high resolution in the boundary layer region. Grid stretching is applied toward the outer domain to reduce computational cost while maintaining accuracy. With refined elements near the cylinder surface to accurately resolve boundary layer dynamics. Figure 5 presents the grid topology used for the validation case at Re = 3900, which is consistent with previous high-fidelity LES studies and supports the accuracy of the simulation framework.

Analysis of end-face effects on finite-length cylinders

Near the upper and lower end faces of the cylinder, the flow field distribution differs from that in the middle section of the cylinder. The height of the cylinder is divided into multiple small sections along the height direction (z-direction) to analyze the distribution pattern of the drag coefficient of the cylinder along the height direction, as shown in Figure 6:

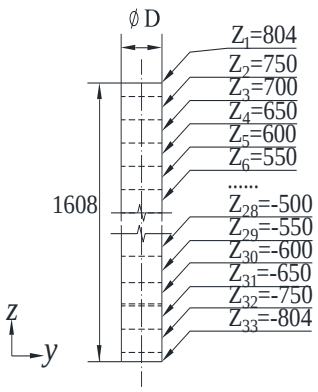

Fig. 6. - Schematic diagram of various cross-sections of the cylinder (unit: mm)

The temporal variation of the drag coefficient for sections Z_1, Z_2, ..., Z_{31}, Z_{32}, Z_{33} of the cylinder under different operating conditions is calculated. This is illustrated in Figures 7 to 10, where *Re* is respectively 10^4, 10^5, 2.5×10^5, 5×10^5. The primary sections affected by end-face effects are Z_1, Z_2, Z_{31}, Z_{32}, and Z_{33}. The temporal variation patterns of the drag coefficient for sections in the middle of the cylinder (sections Z_4, Z_5, ..., Z_{30}) are relatively consistent and are collectively referred to as the "UA" (Undisturbed Area) region.

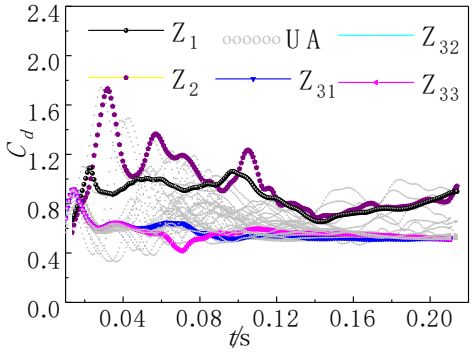

Fig. 7 - The drag coefficients for each section when Re=10⁴

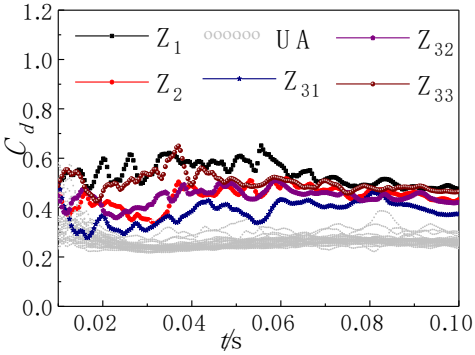

Fig. 8 - The drag coefficients for each section when Re=10⁵.

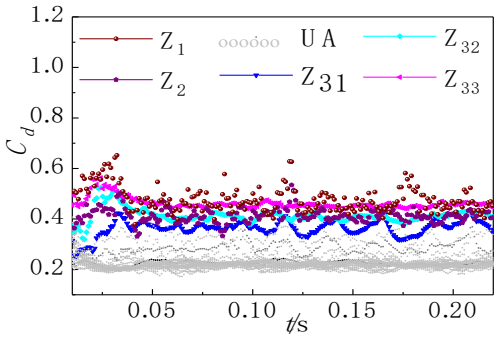

Fig. 9 - The drag coefficients for each section when Re=2.5×10⁵.

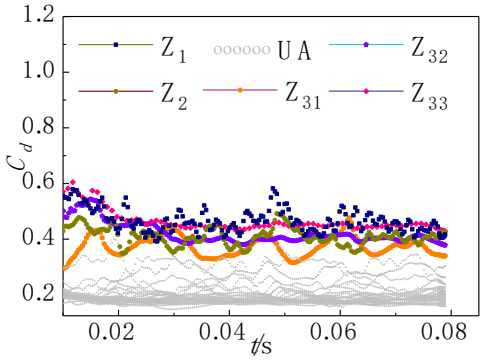

Fig. 10 - The drag coefficients for each section when Re=5×10⁵.

Further analysis reveals the average drag coefficient of the cylinder and each section simulated under different operating conditions, as shown in *Re*=10^4 as an example, the differences between the drag coefficient of sections Z_1-Z_5 and the average drag coefficient of the cylinder are 32.70%, 35.97%, 14.46%, 5.85%, and 4.82% respectively. Similarly, the differences between the drag coefficient of sections Z_{29}-Z_{33} and the average drag coefficient of the cylinder are 3.93%, 6.20%, 25.98%, 36.49%, and 39.24% respectively.

Analysis of end-face effects on finite-length variable diameter cylinders

The flow field distribution varies notably between the central section and the vicinity of the upper and lower end faces of the cylinder. In the derivation of the drag for finite-length variable diameter cylinders, as illustrated in Figure 3, it's approximated that the cylinder consists of an infinite number of infinitesimal cylinders, each with the same drag coefficient. Hence, the drag F_X of the variable diameter cylinder can be

expressed as follows:

$$F_x = \sum F_{xi} = C_{d1}\frac{1}{2}\rho V^2 \Delta H_1 d_1 + C_{d2}\frac{1}{2}\rho V^2 \Delta H_2 d_2 + ... + C_{dn}\frac{1}{2}\rho V^2 \Delta H_n d_n = \frac{1}{2}\rho V^2 \Delta H \sum C_{di} d_i \quad (18)$$

In the equation above, it's assumed that the drag on each section of the cylinder is uniform, neglecting the flow field changes around the cylinder's upper and lower end faces. Additionally, there's an angle between the side characteristic line and the central line of the variable diameter cylinder. The derivation treats each section of the variable diameter cylinder as a cylinder, leading to discrepancies between the derived drag formula and experimental results. These factors need detailed analysis. Parameters affecting the drag F_X of the variable diameter cylinder include the angle θ between the side characteristic line and the central line (expressed as $\tan\theta$), Reynolds number *Re*, height *H*, diameter *D* (expressed as the height-to-diameter ratio $\lambda = (H/D)$), or considering the windward area A. Thus, the drag of the variable diameter cylinder can be represented by the following equation:

$$F_x = \frac{1}{2}\rho V^2 C_d A \quad (19)$$

Wherein:

$$F_x = \frac{1}{2}\rho V^2 C_d A \quad (20)$$

$$C_d = f(Re, \frac{H}{D}) \quad (21)$$

Calculation model and computational conditions

The distance from the model to the boundary of the computational domain is shown in Figure 11, meeting the requirement of eliminating the influence of computational domain scale on the flow field. Grid division is based on different cylinder models, with a total number of grids ranging from 9 to 11 million. The near-wall functions method is used to solve near the surface of the cylinder, and the inlet velocity magnitude is determined based on *Re* and the characteristic size of the cylinder.

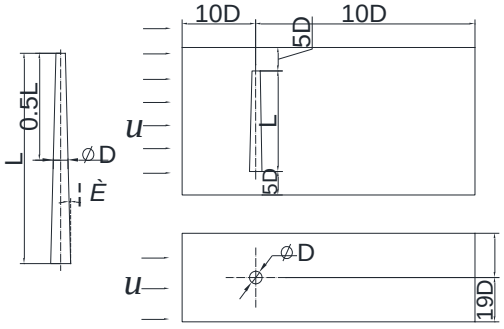

Fig. 11 - Variable diameter cylinder model and computational domain.

Numerical simulation results and analysis

Further analyze the influence of end effects on the drag coefficient. Within three different (*Re*) ranges, variable diameter cylinder models are established to numerically simulate and calculate the sectional drag coefficients. The parameters of the variable

diameter cylinder model are selected as follows: upper diameter of 31.34mm, lower diameter of 118.66mm, height-to-diameter ratio of 13.33, and inclination angle (θ) of 2.5°.

The error between the drag values derived from the variable diameter cylinder formula and those obtained from numerical simulations ranges from 13% to 16%, indicating a need for correction. Hence, a variable-diameter cylinder characterized by Reynolds number *Re*, the angle *θ* between the side characteristic line and the midline, length *H*, and mid-diameter *D* is established. The model parameters, comprehensively considering the factors affecting the end-face effect of the flow around the variable-diameter cylinder, are as follows: *Re*= 5×10^4 ~ 8×10^4 ,*D*=50~75mm,*H*=650~1000mm, θ =2~5° ; *Re*= 1.25×10^5 ~ 2.5×10^5 ,*D*=50mm~85mm,*θ*=2°~6°;*Re*= 4.5×10^5 ~ 5×10^5 ,*D*=50mm~75mm,*θ*=1°~6°.A total of 21 operating conditions were considered.

Tab.2 - Error between formula derivation and numerical simulation

Reynolds number	Drag			Drag coefficient		
	Formula derivation	Numerical simulation	Error (%)	Formula derivation	Numerical simulation	Error(%)
5×10^4	6.35	7.22	13.77	0.53	0.66	13.77%
2.5×10^5	126.00	141.22	12.08	0.61	0.68	12.08%
5×10^5	173.27	200.41	15.64	0.35	0.40	15.64%

In the analysis process, the positions of each section are represented by the distance in the z-axis direction of the variable diameter cylinder, using the same representation method as shown in Figure 2. In Figure 12 to 16, the sections with distinct characteristics are displayed, while other more concentrated sections are defined as the Concentration Area (CA) region. The non-steady variation of the drag coefficient within different regions is calculated through numerical simulations.

Analyzing the variation of the drag coefficient within the, the drag recovery region under constant Reynolds number (*Re*), with respect to the changes in *θ* and *λ*. Figure 12 shows the coefficient curves of the drag fluctuation characteristics for various sections of the variable diameter cylinder, with $Re=5\times10^4$, *θ* values of 3.5° and 5°, and *λ* values of 13.3 and 10. From Figure 12, it can be observed that as *θ* increases, the distance affected by the upper base of the variable diameter cylinder increases, while the distance affected by the lower base remains relatively consistent. The intermediate sections are unaffected, exhibiting consistent drag coefficients.

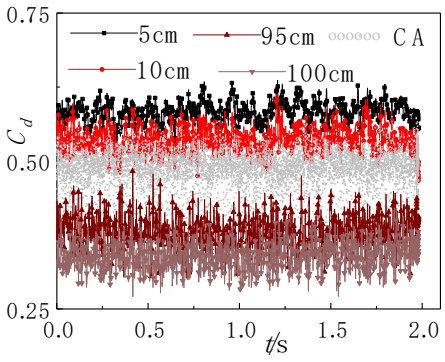

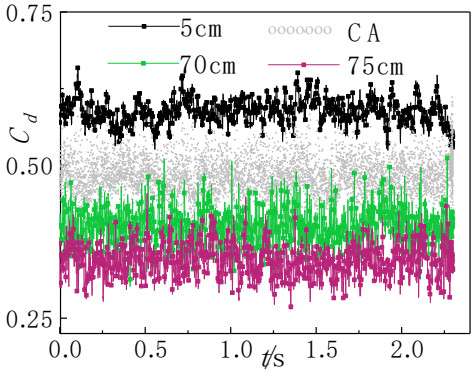

(a) $Re=5\times10^4$, λ=13.3, θ=3.5° (b) $Re=5\times10^4$, λ=10, θ=5°

Fig. 12- Drag coefficient for various sections of $Re=5\times10^4$, λ=9.3 and 10, θ=3° and 5°.

Analyzing the drag crisis region, under constant *Re* conditions, the variation pattern of the drag coefficient with θ and λ. Figure 13 shows the coefficient of drag fluctuation characteristics for various sections when $Re=8\times10^4$, λ is 13.3 and 10, and θ is 3.5° and 5°. Due to the influence of the angle θ and the end effect on the flow field, as Re decreases, the non-uniformity of the distribution along the centerline direction further increases. At the same time, for higher Re conditions ($Re=5\times10^5$), the influence of the end effect on the bottom and top of the variable diameter cylinder is further intensified, enhancing the stability of the drag coefficient.

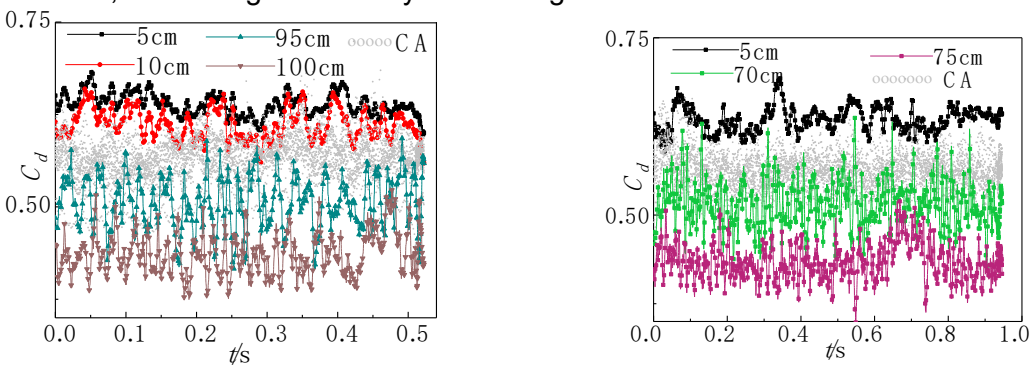

(a) $Re=8\times10^4$, λ=13.3, θ=3.5° (b) $Re=8\times10^4$, λ=10, θ=5°

Fig. - 13 Drag coefficient for various sections of $Re=8\times10^4$, λ=13.3 and 10, θ=3.5° and 5°.

Analysis of the drag recovery region, with *Re* remaining constant, the variation of the resistance coefficient with θ and λ. Figure 14 shows the fluctuation characteristics of the resistance coefficient curves for different sections when $Re=4\times10^5$, λ is 9.3 and 13.3, and θ is 6° and 2°. It can be observed from Figure 14 that when the Reynolds number Re is the same and θ is relatively large, the range of the influence of the end-face effect on the variable-diameter cylinder in the axial direction increases. This effect is particularly pronounced when θ is 6°. Analyzing the resistance coefficient crisis zone, with Re remaining constant, the variation of the resistance coefficient with θ and λ. Figure 14(b) shows the resistance coefficient curves of various sections when $Re=1.25\times10^5$, θ is 2° and, and λ is 13.3. Combined with the analysis of Figure 14(a), it can be observed that when θ is small, the range of influence on the top and bottom ends of the variable-diameter cylinder decreases, and the difference between the resistance coefficients of sections affected and unaffected by the end-face effect can be more clearly distinguished.

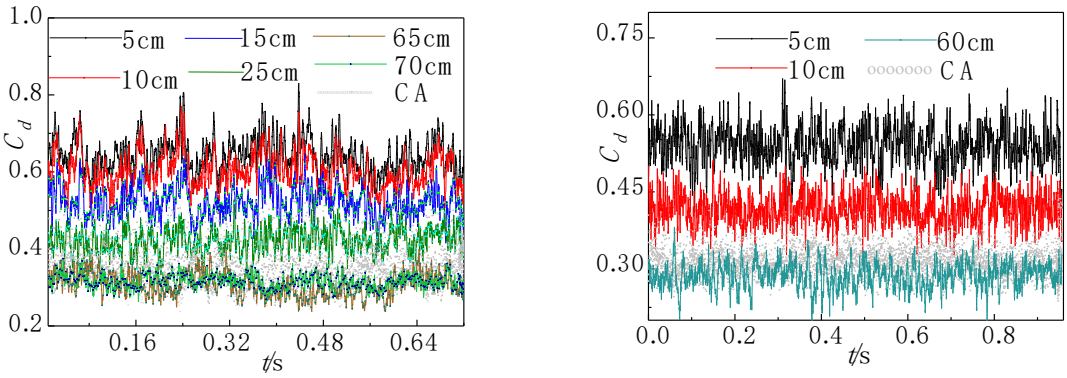

(a) $Re=2.5\times10^5$, λ=9.3, θ=6° (b) $Re=1.25\times10^5$, λ=13.3 . , θ=2°

Fig. 14 - Drag coefficient for various sections of $Re=2.5\times10^5$ and $Re=1.25\times10^5$, λ=9.3 and 13.3,θ=6° and 2°.

In the drag crisis region, with *Re* remaining constant, the variation of the resistance coefficient with θ and λ is analyzed. Figure 15 depicts the fluctuation characteristics of the resistance coefficient of each section under conditions $Re=2.5\times10^5$, $Re=5\times10^5$, θ=4° and 6°, and λ=9.4 and 9.3. It can be observed that with the increase of θ, the resistance coefficient near the upper end of the variable-diameter cylinder undergoes significant changes, showing a large difference compared to the resistance coefficient near the middle section. Figure 16 shows the resistance coefficients of each section under conditions $Re=4.5\times10^5$ and $Re=8\times10^4$, with θ =4° and 6°, and λ =9.4 and 9.3. When θ increases to 6°, the resistance coefficient near the upper end of the variable-diameter cylinder undergoes changes. Under the same θ and λ, the difference between the resistance coefficient in the affected range and the average resistance coefficient is minimized when $Re=1.25\times10^5$.

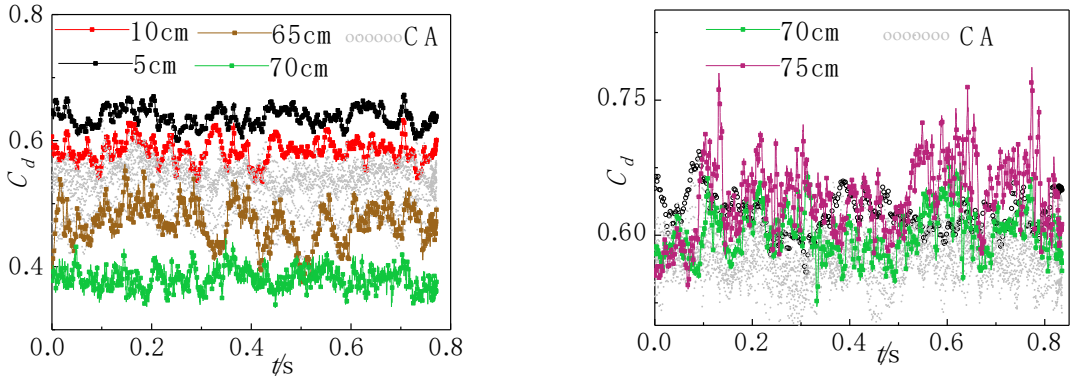

(a) $Re=2.5\times10^5$, λ=9.4, θ=4° (b) $Re=5\times10^5$, λ=9.3, θ=6°

Fig. 15 - Drag coefficient for various sections of $Re=2.5\times10^5$ and $Re=5\times10^5$, λ=9.4 and 9.3,θ=4° and 6°.

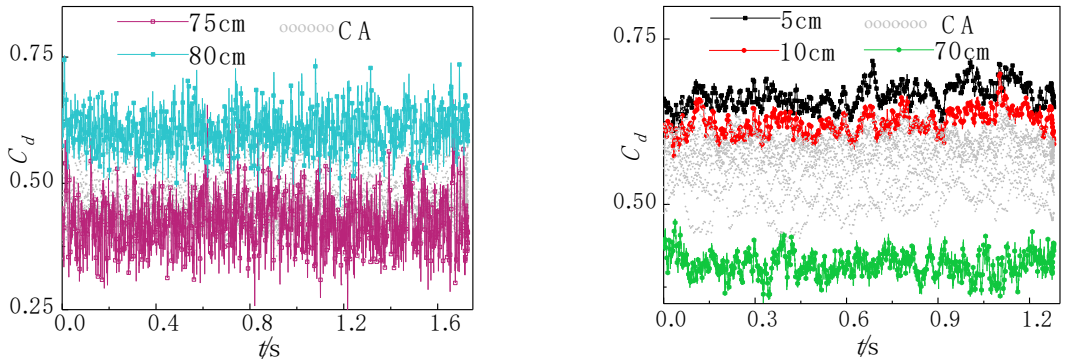

(a) $Re=4.5\times10^5$, λ=9.4, θ=4° *(b)* $Re=8\times10^4$, λ=9.3, θ=6°

Fig. 16 - Drag coefficient for various sections of $Re=4.5\times10^5$ *and* $Re=8\times10^4$, *λ=9.4 and 9.3,θ=4° and 6°.*

Based on the comprehensive analysis of the calculation results, further investigation is conducted into the range influenced by the angle *θ* between the side characteristic line and the central line, affecting the resistance coefficient of the upper and lower ends. The range of influence on the upper end of the variable-diameter cylinder due to *θ* and end-face effects is denoted as h_1', where $h_1' = h_1/d_1$ represents the extent of influence on the upper end, and represents the extent of influence on the lower end. Here, $h_1$represents the distance of influence on the upper end along the axis of the variable-diameter cylinder, and $h_2$represents the distance of influence on the lower end. The average resistance coefficient of the variable-diameter cylinder is denoted as C_d, with $C_{d_1}'$and C_{d_2}' representing the resistance coefficients influenced by the upper and lower ends, respectively. $C_{d_1}'$and $C_{d_1}'$are the average values of the resistance coefficients of various sections within distances h_1 and h_2, respectively. Δ_1 and Δ_2 are defined as the errors in the resistance coefficients, where $\Delta_1=\left|(C_{d_1}'-\overline{C_d})/\overline{C_d}\times100\%\right|$ and $\Delta_2=\left|(C_{d_2}'-\overline{C_d})/\overline{C_d}\times100\%\right|$, as shown in Table 3.

Tab.3 - Influence Range and Errors of End-face Effects

Operating condition	Average drag coefficient $\overline{C_d}$	Range of influence		Drag coefficient of the affected cross-section		Drag coefficient error(%)	
		h_1'	h_2'	C_{d_1}'	C_{d_2}'	Δ_1	Δ_2
1	0.503	0.386	0.037	0.419	0.586	16.71	16.40
2	0.497	1.038	0.036	0.371	0.584	25.42	17.44
3	0.570	0.519	0.036	0.437	0.637	23.24	11.88
4	0.799	4.152	0.107	0.686	0.904	14.11	13.18
5	0.576	1.929	0.036	0.525	0.633	8.84	9.89
6	0.790	4.244	0.109	0.706	0.896	10.62	13.41
7	0.612	0.170	0.031	0.692	0.586	15.21	3.96
8	0.591	0.343	0.036	0.624	0.710	5.57	20.14
9	0.461	24.589	0.101	0.338	0.581	26.69	26.12
10	0.494	0.549	0.069	0.527	0.515	6.56	4.21
11	0.349	1.657	0.138	0.307	0.475	12.08	36.16
12	0.634	0.171	0.036	0.751	0.661	18.50	4.32
13	0.465	0.1712	0.036	0.561	0.609	20.76	30.96
14	0.602	8.196	0.034	0.472	0.674	21.59	11.84
15	0.554	8.196	0.034	0.432	0.638	21.96	15.10
16	0.567	0.258	0.082	0.709	0.539	25.04	4.93
17	0.503	0.517	0.082	0.545	0.514	8.41	2.39
18	0.521	0.232	0.039	0.569	0.671	2.98	15.5
19	0.458	1.173	0.134	0.386	0.599	14.57	22.98
20	0.615	0.130	0.045	0.643	0.657	4.64	6.85
21	0.578	0.261	0.045	0.597	0.680	3.35	17.64

Further analysis of the influence range h_1' and h_2' of end-face effects with respect to the Reynolds number Re, aspect ratio λ, and the angle θ between the side characteristic line and the central line, with h' representing the comprehensive influence range.

$$h' = -162.939 - 13.555\ln(Re) + 7.309\tan\theta + 61.041\lambda + 6.268\ln^2(Re) \\ -3.264\tan^2\theta - 6.959\lambda^2 - 0.773\ln^3(Re) + 0.420\tan^3\theta + 0.249\lambda^3 \quad (22)$$

Compared to a straight circular cylinder, the angle θ is the primary factor influencing the resistance coefficient of a variable-diameter cylinder. Due to the flow disturbances caused by θ and the end-face effects induced by the cylinder's flow, the distribution pattern of resistance is further complicated. Therefore, the sections near the upper and lower bases are analyzed separately to study the resistance coefficient's temporal variation and average value along different sections. Subsequently, the sections with consistent patterns are combined to obtain an average value, representing the comprehensive height h' affected by the end faces. Through data fitting, a specific form of the resistance correction formula can be constructed as follows:

$$F_z' = a_0 + bRe + c_1\lambda + m\tan\theta \quad (23)$$

Based on the results obtained from Table 3, the coefficients for the correction terms can be calculated, taking into account the different zones.

(1) When $10^4 \le Re < 10^5$, Subcritical region

$$F_{z1}' = -0.044 - 4.800\ln(Re) + 2.279\lambda^{-1} - 3.131\tan\theta \quad (24)$$

(2) When $10^5 \le Re < 4\times10^5$, Drag crisis region

$$F_{z2}' = -3.102 - 0.307\ln(Re) + 1.149\lambda^{-1} - 8.558\tan\theta \quad (25)$$

(3) When $Re \ge 4\times10^5$, Drag recovery region

$$F_{z3}' = -3.291 + 1.003\ln(Re) + 1.194\lambda^{-1} + 3.363\tan\theta \quad (26)$$

Equations (24) to (26) are appended to equations (10) to (12), resulting in the final modified variation pattern of the variable-diameter cylinder's resistance. Through the correction equations above, the corrected error within the three resistance zones ranges from 1.5% to 9.34%, meeting the practical engineering requirements.

CONCLUSION

1. This study presents a comprehensive investigation into the flow resistance characteristics of finite-length variable diameter cylinders across subcritical, drag crisis, and drag recovery regimes. Through Large Eddy Simulation (LES), we quantified how aspect ratio, Reynolds number, and side angle influence drag distributions, especially near cylinder ends. A key contribution of this work is the derivation of a segmented drag coefficient model and an end-effect correction formula that significantly reduces predictive error.

2. The simulation results showed that drag coefficients vary notably at the cylinder extremities, with up to 39.24% deviation from the mean value observed. The proposed correction formula successfully reduces these deviations to below 9.34%, thus enhancing accuracy for practical applications. Furthermore, we provide a parametric formula that relates the end-effect influence range to geometric and flow conditions, offering a generalized approach for integrating end effects in engineering analyses.

3. Although direct experimental validation is limited in this study, our numerical approach is benchmarked against established experimental data for Re = 3900, showing excellent agreement. Future work will focus on wind tunnel experiments and pressure tap measurements to further validate the model predictions. The findings of this study are especially valuable in the design and analysis of civil and energy-related structures involving tapered cylindrical components.

ACKNOWLEDGEMENTS

This research was funded by Natural Science Foundation of Inner Mongolia Autonomous Region. Awaed Number: No,2023LHMS01010; Basic scientific research business fee project for directly affiliated universities in Inner Mongolia Autonomous Region JY20240056.16

REFERENCES

[1] Xu, Y.; Chen, S., Analysis of flow characteristics around a rotating cylinder. Chinese Journal of Theoretical and Applied Mechanics 2021, 53, (7), 1900-1911. DOI:https://doi.org/10.6052/0459-1879-21-153

[2] Yang, F.; Zhou, Z.; Lou, X.; Lu, L., Flow around a near-bed horizontal circular cylinder mounted on a vertical wall. Ocean Engineering 2020, 216, 107586.

[3] Morton, C.; Yarusevych, S., Vortex shedding from cylinders with two step discontinuities in diameter. Journal of Fluid Mechanics 2020, 902. DOI:https://doi.org/10.1017/jfm.2020.593

[4] Wang, L.; Lei, L.; T.; Zheng, K.; Guo, J., Investigation on the flow-induced vibration of tandem cylinders with varying diameters at subcritical Reynolds numbers. Applied Ocean Research 2023. DOI:https://doi.org/10.1016/j.apor.2023.103669

[5] Gu, H.; Guo, H.; Li, X.; Li, F., Experimental investigation into the effect of diameter ratio on the flow-induced vibration of tandem flexible cylinders. Ocean Engineering 2023. DOI:https://doi.org/10.1016/j.oceaneng.2023.115978

[6] Khan, A.; Sanaullah, K.; Khan, S.; Rigit, A.; Ullah, A., Hydrodynamics of the steam-water two-phase flows behind a pair of bluff cylinderical bodies inside and around the wake region. Proceedings of the Institution of Mechanical Engineers, Part C: Journal of Mechanical Engineering Science 2020, 235, (19), 3923-3932. DOI:https://doi.org/10.1177/0954406220971672

[7] Nazvanova, A.; Yin, G.; Ong, M.C. Numerical Investigation of Flow around Two Tandem Cylinders in the Upper Transition Reynolds Number Regime Using Modal Analysis. J. Mar. Sci. Eng. 2022, 10,1501.DOI:https://doi.org/10.3390/jmse10101501

[8] Zhao, L. S.; Wei, Z. J.; Lei, M., Experiments and numerical simulations of the three-dimensional flow around a finite-length circular cylinder. SHIP SCIENCE AND TECHNOLOGY 2021, 43, (11), 19-24.

[9] Tong, X.J. Numerical Simulation Study on the Flow Characteristics around a Cylinder at Low Reynolds Numbers Based on Fluent. Master's thesis, Yangzhou University, Yangzhou, China, 2021.

[10] Zhao, G.; Gui, H.; Wang, X., Numerical simulation of flow around finite-length wavy cylinders. Journal of Harbin Institute of Technology 2021, 53, (6), 163-170. DOI:https://doi.org/10.11918/201909017

[11] Hao, L.; Chen, L.; Ni, M., Direct numerical simulations on the turbulent flow past a confined circular cylinder with the influence of the streamwise magnetic fields. Chinese Journal of Theoretical and Applied Mechanics 2020, 52, (6), 1645-1654. DOI:https://doi.org/10.6052/0459-1879-21-153

[12] Gao, Y.; Yang, S.; Wang, L.; Huan, C.; Zhang, J. Numerical Investigation on Vortex-Induced Vibrations of Two Cylinders with Unequal Diameters. J. Mar. Sci. Eng. 2023, 11, 377. DOI:https://doi.org/10.3390/jmse11020377

[13] Nelson, D. A.; Jacobs, G. B.; Kopriva, D. A., Effect of boundary representation on viscous, separated flows in a discontinuous-Galerkin Navier–Stokes solver. Theoretical and Computational Fluid Dynamics 2016, 30, (4), 363-385. DOI:https://doi.org/10.1007/s00162-016-0388-7

[14] Li, Y. C.; Peng, S.; Kouser, T., Effect of wall slip on laminar flow past a circular cylinder. Acta Mechanica 2022, 233, (10), 3957-3975. DOI:https://doi.org/10.1007/s00707-022-03297-1

[15] Sufyan, M.; Manzoor, S.; Sheikh, N. A., Heat Transfer Suppression in Flow Around a Rotating Circular Cylinder at High Prandtl Number. Arabian Journal for Science and Engineering 2014, 39, (11), 8051-8063. DOI:https://doi.org/10.1007/s13369-014-1337-7

[16] Giedt., Effect of Turbulence Level of Incident Air Stream on Local Heat Transfer and Skin Friction on a Cylinder. Journal of the Aeronautical Sciences 1951, 18, (11), 725-730.
[17] Wu, W. C.; Han, X. S.; Mao, J. K., Large Eddy Simulation of Flow Around a D-Shaped Bluff Body for Drag Reduction Based on Passive Control. Journal of Propulsion Technology 2020, 41, (8), 1692-1700. DOI:https://doi.org/10.13675/j.cnki.tjjs.190405
[18] McClure, J.; Morton, C.; Yarusevych, S., Flow development and structural loading on dual step cylinders in laminar shedding regime. Physics of Fluids 2015, 27, (6). DOI:https://doi.org/10.1063/1.4921491
[19] Kravchenko, A. G.; Moin, P., Numerical studies of flow over a circular cylinder at ReD=3900. Physics of Fluids 2000, 12, (2), 403-417. DOI:https://doi.org/10.1063/1.870318
[20] Wu, W. C.; Han, X. S.; Mao, J. K., Large Eddy Simulation of Flow Around a D-Shaped Bluff Body for Drag Reduction Based on Passive Control. Journal of Propulsion Technology 2020, 41, (8), 1692-1700. DOI:https://doi.org/10.13675/j.cnki.tjjs.190405
[21] Meng, Z.; yu, L. X.; Yan, J.; he, W. Y., Research on the Large Eddy Simulation Past Flow Around Single and Ddouble Cylinderical-Like Objects. Machinery Design & Manufacture 2019, (11), 126-132. DOI:https://doi.org/10.19356/j.cnki.1001-3997.2019.11.033
[22] Du, X.; Jiang, B.; Dai, C.; Wang, G.; Chen, S., Experimental study on wake-induced vibrations of two circular cylinders with two degrees of freedom. Wind and Structures, An International Journal 2018, 26, (2), 57-68. DOI:https://doi.org/10.12989/was.2018.26.2.057